Intense microwave generation from a non-neutral rotating E layer

W. W. Destler, H. Romero, C. D. Striffler, R. L. Weiler, and W. Namkung
Electrical Engineering Department, University of Maryland, College Park, Maryland 20742

(Received 28 July 1980; accepted for publication 10 November 1980)

The radiation produced by a hollow, non-neutral, rotating, relativistic E layer propagating inside a coaxial cylindrical drift tube has been investigated theoretically and experimentally. The measured radiation spectrum is very broadband in agreement with theory, though a shift in the spectrum can be achieved by a preloaded azimuthal density structure.

PACS numbers: 52.80.Vp, 52.60. + h,

I. INTRODUCTION

The production of very-high-power bursts of microwave radiation by coupling the output of high-current relativistic electron accelerators to conventional microwave devices (Klystrons, Backward Wave Oscillators, and Magnetrons) has been reported by several groups during the past few years.[1-5] Many of these experiments have reported conversion efficiencies of electron beam power to microwave power comparable to those achieved in conventional devices working at much lower power levels. The successful application of high-power electron accelerators for the efficient generation of microwave radiation has led to the investigation of several new concepts aimed at intense microwave and millimeter wave production. These new concepts are designed to produce radiation at frequencies attractive for such diverse applications as plasma heating and atmospheric propagation. These new ideas include gyrotrons,[6] free-electron lasers,[7] and radiation from nonneutral rotating E layers,[8,9] the subject of this report.

The loss of electron energy to radiation in rotating electron rings and E layers has been reported by several groups during the past decade,[10-12] usually as part of studies aimed at reducing this radiated energy in order to maintain beam quality. In the work reported here, theory and experiment undertaken with the goal of characterizing and maximizing the microwave radiation from such rotating E layers is reported. Initial studies of the microwave radiation from a rotating E layer were reported by Granatstein *et al.*,[8] and a theoretical analysis of the resonant interaction between beam modes and the TE and TM modes of the vacuum drift chamber in such a system were reported by Sprangle.[13] A more complete experimental study of this radiation production (and its suppression when so desired) was reported by Destler *et al.*,[9] and subsequent theoretical analysis has been provided by several groups.[14,15]

In Fig. 1, a schematic is shown of the experimental system that is used in our studies of microwave generation. The diode is composed of a thin annular cathode of mean radius 6 cm and an anode plate through which the beam passes into the cusped magnetic field. The nominal diode properties are 2-MV, 20–30-kA, and 20–30-ns pulse width. The cusped magnetic field is formed by oppositely driven current coils and an iron plate. A typical axial magnetic field profile is shown in Fig. 1 where we see the field is essentially uniform in a region immediately downstream of the cusp. After passage through the cusp, the hollow rotating E layer has nominal properties of 2-MeV particle energy, 1–2-kA, and 5–10-ns pulse width. The beam is radially thin and axially long because the magnetic field setting is generally 50 G or so below the cutoff magnetic field. Since the beam is fairly tenuous, the rotating azimuthal velocity is that of axis-encircling cyclotron motion,

$$v_{\phi 0} = r_0\omega_c = r_0 eB_0/m\gamma_0, \tag{1}$$

where r_0 is the cathode radius, B_0 the uniform downstream magnetic field, and γ_0 the relativistic mass ratio, i.e., $mc^2(\gamma_0 - 1) = eV_0 \simeq 2$ MeV. The axial velocity depends on the magnetic field setting, and for balanced cusped fields is given by

$$v_{z0}/c = [(\gamma_0^2 - 1)/\gamma_0^2 - (r_0 eB_0/mc\gamma_0)^2]^{1/2}, \tag{2}$$

from which we see a "cutoff" field of

$$B_{0c} = (mc/er_0)(\gamma_0^2 - 1)^{1/2}. \tag{3}$$

The post cusp hollow beam propagates down a coaxial waveguide system formed by inner and outer conducting cylindrical walls between which the E layer travels. We theorize that the beam forms azimuthal clumps due to the negative mass effect, and subsequently radiates as coherent synchrotron radiation. The radiation is seen at the end of the waveguide when the frequency of such radiation is above the cutoff frequency of the cylindrical waveguide system. Further-

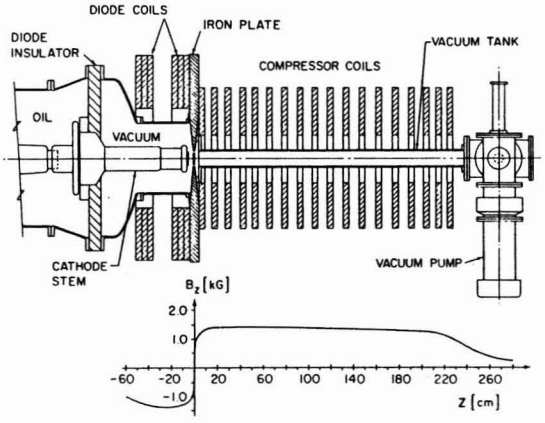

FIG. 1. Schematic of the University of Maryland rotating E layer microwave generation system.

 0021-8979/81/042740-10$01.10

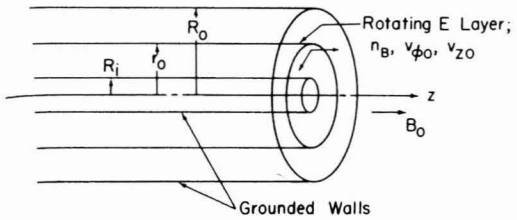

FIG. 2. Geometry of the model.

more, we expect an enhancement of radiation at frequencies associated with the various waveguide modes.

In this paper, a theoretical treatment identical in formalism to Sprangle[13] of the linear stability of a thin, dilute, rotating E layer propagating in a coaxial waveguide system is presented in Sec. II. Results of experimental studies of the radiation production in such a system are presented in Sec. III. Conclusions are drawn in Sec. IV.

II. THEORY

To study some of the properties associated with microwave generation from a rotating E layer traveling in a coaxial waveguide system, we consider the model whose geometry is shown in Fig. 2. The coaxial waveguide consists of ideal inner and outer concentric cylindrical conducting walls of radii R_i and R_0, respectively. The thin E layer of radius r_0 is concentric with the conducting cylinders and has a mean azimuthal velocity $v_{\phi 0} = \beta_{\phi 0} c$ and mean axial velocity $v_{z0} = \beta_{z0} c$ and a relativistic mass ratio $\gamma_0 = (1 - \beta_{\phi 0}^2 - \beta_{z0}^2)^{-1/2}$. The entire system is immersed in a uniform axial magnetic field B_0.

We examine the linear electromagnetic stability of this system in the limit of a tenuous beam at the condition for resonant interaction between a beam wave and the various TE and TM modes of the coaxial cylindrical waveguide. Such an interaction can be depicted as shown in Fig. 3, where a typical waveguide mode and beam mode are plotted in an ω-k_z diagram. At the interaction points indicated (k_z^-, ω^-) and (k_z^+, ω^+), we have "resonant interaction". If these are both unstable, a backward (ω^-) and forward (ω^+) growing wave are produced. If no intersection of the two modes occurs, then a resonant interaction is not possible and the proceeding analysis will indicate no unstable wave. This is not to imply that only resonant interactions are unstable but to indicate the properties of such unstable interactions by analyzing the relatively simple resonant interaction.

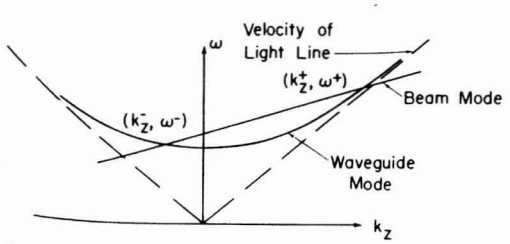

FIG. 3. Graphical description of resonant interaction between a waveguide mode and a beam mode.

The basic equations used in examining the linear electromagnetic stability of the system are the single particle orbit equations and Maxwell's equations. These equations are, respectively,

$$m \frac{d}{dt} \gamma \mathbf{v} = -e(\mathbf{E} + \mathbf{v} \times \mathbf{B}) \tag{4}$$

and

$$\left(\nabla^2 - \frac{1}{c^2} \frac{\partial^2}{\partial t^2}\right) \mathbf{E} = \mu_0 \frac{\partial \mathbf{J}}{\partial t} + \frac{1}{\epsilon_0} \nabla \rho, \tag{5a}$$

$$\left(\nabla^2 - \frac{1}{c^2} \frac{\partial^2}{\partial t^2}\right) \mathbf{B} = -\mu_0 \nabla \times \mathbf{J}, \tag{5b}$$

where m, $-e$ are the rest mass and charge of a beam electron, $\gamma = (1 - \beta_r^2 - \beta_\phi^2 - \beta_z^2)^{-1/2}$ is the relativistic mass ratio with $v_r = \beta_r c = \dot{r}$, $v_\phi = \beta_\phi c = r\dot{\phi}$, $v_z = \beta_z c = \dot{z}$ as the velocity components in cylindrical coordinates, (r,ϕ,z),$\mathbf{E}$,$\mathbf{B}$ are the electric and magnetic fields in the system, and ρ,$\mathbf{J}$ are the beam charge and current densities.

The *equilibrium* steady-state system is described mathematically by the conditions $\partial/\partial t, \partial/\partial\phi, \partial/\partial z = 0$. Under these conditions, plus the assumption of a tenuous beam, that is, the beam self fields are ignorable, Eq. (4) gives the beam equilibrium properties as

$$\begin{aligned} &v_r \equiv v_{r0} = 0, \\ &v_\phi \equiv v_{\phi 0} = (eB_0/m\gamma_0) r_0 = \Omega_0 r_0/\gamma_0 = \omega_c r_0, \\ &v_z \equiv v_{z0}, \end{aligned} \tag{6}$$

and

$$\gamma \equiv \gamma_0 = (1 - \beta_0^2)^{-1/2} = (1 - \beta_{\phi 0}^2 - \beta_{z0}^2)^{-1/2},$$

where B_0 is the uniform applied axial magnetic field. We further assume that the beam is thin such that the beam density is given by $n_b = n_s \delta(r - r_0)$, where n_s is the surface particle density of the beam. Thus our system is a thin, tenuous rotating E layer that also propagates along an applied magnetic field between two concentric coaxial conductors of radii R_i,R_0, as shown in Fig. 2.

The *stability* of the system is examined by linearizing Eqs. (4) and (5). The orbit equation is linearized as

$$\begin{aligned} &r = r_0 + r_1(\phi,z,t), \\ &\phi = \phi_0 + (\Omega_0/\gamma_0)t + \phi_1(\phi,z,t), \\ &z = z_0 + v_{z0} t + z_1(\phi,z,t), \end{aligned} \tag{7}$$

where subscript "one" variables are assumed small compared to subscript "zero" (equilibrium) values. The linearized particle velocities become

$$\begin{aligned} &v_{r1} = \dot{r}_1, \\ &v_{\phi 1} = r_0 \dot{\phi}_1 + (\Omega_0/\gamma_0) r_1, \\ &v_{z1} = \dot{z}_1. \end{aligned} \tag{8}$$

Linearizing the electric and magnetic fields as

$$\begin{aligned} &\mathbf{E} = \delta\mathbf{E}(r,\phi,z,t), \\ &\mathbf{B} = B_0 \hat{\mathbf{z}} + \delta\mathbf{B}(r,\phi,z,t), \end{aligned} \tag{9}$$

Fourier decomposing in the ϕ,z,t coordinates as $\exp i(l\phi + k_z z - \omega t)$, the linearized particle positions become

$$\tilde{r}_1 = \frac{e}{m\gamma_0 D_l^2}\left(\psi_l^2\,\overline{\delta E_r} + i\psi_l\frac{\Omega_0}{\gamma_0}\,\overline{\delta E_\phi} + i\psi_l\frac{\Omega_0}{\gamma_0}\beta_{z0}c\,\overline{\delta B_r} - \psi_l^2\beta_{z0}c\,\overline{\delta B_\phi} + \psi_l^2\beta_{\phi 0}c\,\overline{\delta B_z}\right), \tag{10a}$$

$$r_0\tilde{\phi}_1 = \frac{ie}{m\gamma_0 D_l^2}\left[-\psi_l\frac{\Omega_0}{\gamma_0}\,\overline{\delta E_r} - i\left(\frac{\psi_l^2}{\gamma_{\phi 0}^2} + \frac{\Omega_0^2}{\gamma_0^2}\beta_{\phi 0}^2\right)\overline{\delta E_\phi} + i\beta_{\phi 0}\beta_{z0}\left(\psi_l^2 - \frac{\Omega_0^2}{\gamma_0^2}\right)\overline{\delta E_z}\right.$$

$$\left. - i\beta_{z0}c\psi_l^2\,\overline{\delta B_r} + \psi_l\frac{\Omega_0}{\gamma_0}\beta_{z0}c\,\overline{\delta B_\phi} - \psi_l\frac{\Omega_0}{\gamma_0}\beta_{\phi 0}c\,\overline{\delta B_z}\right], \tag{10b}$$

and

$$\tilde{z}_1 = (e/m\gamma_0\psi_l^2)(\,\overline{\delta E_z}/\gamma_{z0}^2 - \beta_{z0}\beta_{\phi 0}\,\overline{\delta E_\phi} - \beta_{\phi 0}c\,\overline{\delta B_r}), \tag{10c}$$

where

$$D_l^2 = \psi_l^2(\psi_l^2 - \Omega_0^2/\gamma_0^2), \quad \psi_l = \omega - l\Omega_0/\gamma_0 - k_z v_{z0},$$
$$\gamma_{z0}^2 = (1-\beta_{z0}^2)^{-1}, \quad \gamma_{\phi 0}^2 = (1-\beta_{\phi 0}^2)^{-1},$$

and the variables with bar or tildes represent the Fourier-decomposed amplitude that depend on r. In the same way, the z component of the linearized Maxwell equations becomes

$$\left(\frac{\partial^2}{\partial r^2} + \frac{1}{r}\frac{\partial}{\partial r} - \frac{l^2}{r^2} + \frac{\omega^2}{c^2} - k_z^2\right)\overline{\delta E_z}$$
$$= -i\mu_0\omega\,\overline{\delta J_z} + i\frac{k_z}{\epsilon_0}\,\overline{\delta\rho}, \tag{11a}$$

$$\left(\frac{\partial^2}{\partial r^2} + \frac{1}{r}\frac{\partial}{\partial r} - \frac{l^2}{r^2} + \frac{\omega^2}{c^2} - k_z^2\right)\overline{\delta B_z}$$
$$= -\mu_0\left(\frac{1}{r}\frac{\partial}{\partial r}r\,\overline{\delta J_\phi} - \frac{il}{r}\,\overline{\delta J_r}\right), \tag{11b}$$

where, with the aid of the continuity equation, the linearized charge and current densities are given by

$$\delta\rho = \tilde{\sigma}_1\delta(r-r_0) + en_s\delta'(r-r_0)\tilde{r}_1, \tag{12a}$$

$$\mathbf{\delta J} = -en_s\delta(r-r_0)\tilde{\mathbf{v}}_1 + \tilde{\sigma}_1\delta(r-r_0)\mathbf{v}_0 + en_s\delta'(r-r_0)\tilde{r}_1\mathbf{v}_0, \tag{12b}$$

with

$$\tilde{\sigma}_1 = en_s\left(\frac{\psi_l - l\Omega_0/\gamma_0}{\psi_l}\frac{\tilde{r}_1}{r_0} + il\tilde{\phi}_1 + ik_z\tilde{z}_1\right). \tag{13}$$

In our analysis, we apply the continuity equation for the prescribed particle motion, whereas in Ref. 13 an independent charge conservation relationship is derived. This difference first appears in Eq. (13) where our coefficient of $\tilde{r}_1/r_0$ is replaced by "1" in the Ref. 13 analysis. In the final results for growth rates [Eqs. (21) and (28)], this effect appears in the terms $(1-l^2/x_{ln}^2)^{1/3}$ and $(1-l^2/y_{ln}^2)^{1/3}$, respectively. We find that this factor is not substantial.

The linearized velocity components after Fourier decomposition are

$$v_{r1} \to -i\psi_l\tilde{r}_1,$$
$$v_{\phi 1} \to -i\psi_l r\tilde{\phi}_1 + \frac{\Omega_0}{\gamma_0}\tilde{r}_1, \tag{14}$$
$$v_{z1} \to -i\psi_l\tilde{z}_1.$$

Our procedure for solving these linearized equations is as follows. We assume the perturbed fields are the various TE and TM coaxial waveguide fields, Fourier decomposed. We substitute these fields into both sides of Eq. (11), multiply the equation by the axial component of the field and by rdr, and then integrate from R_i to R_0 to obtain a modified dispersion relation to the empty waveguide due to the presence of the tenuous beam. The following analytical results are obtained.

A. TE coaxial mode

The fields for the TE coaxial waveguide can be determined from the B_z field with $E_z = 0$. This field is given by

$$\delta B_z = \mathscr{C}_l(\alpha_{ln}r/R_0)\exp i(l\phi + k_z z - \omega t), \tag{15}$$

where

$$\mathscr{C}_l(\alpha_{ln}r/R_0) = CJ_l(\alpha_{ln}r/R_0) + DN_l(\alpha_{ln}r/R_0), \tag{16}$$

J_l, N_l are Bessel functions of first and second kind and $(\alpha_{ln}/R_0)^2 = \omega^2/c^2 - k_z^2$. Applying appropriate boundary conditions leads to a determination of the eigenvalues α_{ln}, given by the solution to

$$J_l'(\alpha_{ln})N_l'(\alpha_{ln}R_i/R_0) - J_l'(\alpha_{ln}R_i/R_0)N_l'(\alpha_{ln}) = 0. \tag{17}$$

Thus for each l, $n = 1,2,\ldots$, which represents a radial mode number. Using Eq. (15), computing the other TE fields, E_r, E_ϕ, B_r, B_ϕ, and performing the manipulations as outlined above, the following modified dispersion relation is obtained:

$$\omega^2 - k_z^2c^2 - \alpha_{ln}^2c^2/R_0^2 = (2\omega_b^2/\gamma_0 D_l^2)\epsilon_{ln}^2\left[\overline{A}_{ln}\mathscr{C}_l^2(x_{ln}) + \overline{B}_{ln}\mathscr{C}_l(x_{ln})\mathscr{C}_l'(x_{ln}) + \overline{C}_{ln}\mathscr{C}_l'^2(x_{ln})\right], \tag{18}$$

where

$$\epsilon_{ln}^2 = [\eta_0^2(1-l^2/x_{ln}^2\eta_0^2)\mathscr{C}_l^2(x_{ln}\eta_0) - \eta_i^2(1-l^2/x_{ln}^2\eta_i^2)\mathscr{C}_l^2(x_{ln}\eta_i)]^{-1},$$

$$\overline{A}_{ln} = \left[x_{ln}\psi_l\left(\frac{\Omega_0}{\gamma_0} - l\frac{\omega - k_z v_{z_0}}{x_{ln}^2}\right)\right]^2,$$

$$\overline{B}_{ln} = 2x_{ln}\psi_l\frac{\Omega_0}{\gamma_0}\left(\frac{\Omega_0}{\gamma_0} - l\frac{\omega - k_z v_{z0}}{x_{ln}^2}\right) \times\left(\omega - k_z v_{z0} - \frac{1}{2}\frac{l\Omega_0}{\gamma_0}\right), \tag{19}$$

$$\overline{C}_{ln} = \psi_l^2(\omega - k_z v_{z0})^2 - x_{ln}^2\frac{\Omega_0^2}{\gamma_0^2}\left(\psi_l^2 - \frac{\Omega_0^2}{\gamma_0^2}\right) - l\frac{\Omega_0}{\gamma_0}\left(\frac{\Omega_0}{\gamma_0}\right)^2(\omega - k_z v_{z0}),$$

and

$$\omega_b^2 = e^2n_s/m\epsilon_0 r_0, \eta_0 = R_0/r_0, \eta_i = R_i/r_0, x_{ln} = \alpha_{ln}r_0/R_0.$$

For the specific case of *resonant* beam-waveguide mode interaction, mathematically given by

$$\omega \simeq \omega_0 = l\Omega_0/\gamma_0 + k_z v_{z0} = (k_z^2 c^2 + \alpha_{ln}^2 c^2/R_0^2)^{1/2}, \quad (20)$$

the above dispersion relation can be solved for a growth rate $\Gamma_{TE} \equiv \mathcal{I}m\omega$. The result is

$$\frac{\Gamma_{TE}}{\omega_c(\nu/\gamma_0)^{1/3}} = \frac{\sqrt{3}}{(2\beta_{\phi 0})^{2/3}}\left(\frac{\Omega_0/\gamma_0}{\omega_0}\right)^{1/3} \times \left[|g_{ln}^{TE}|\left(1 - \frac{l^2}{x_{ln}^2}\right)\right]^{1/3}, \quad (21)$$

where

$$g_{ln}^{TE} = -\frac{\pi}{2}x_{ln}^3\left[J_l'\left(\alpha_{ln}\frac{R_i}{R_0}\right)N_l'(x_{ln}) - J_l'(x_{ln})N_l'\left(\alpha_{ln}\frac{R_i}{R_0}\right)\right]\left[J_l'(\alpha_{ln})N_l'(x_{ln}) - J_l'(x_{ln})N_l'(\alpha_{ln})\right] \times \left\{\frac{R_0}{r_0}\left[J_l''(\alpha_{ln})N_l'\left(\alpha_{ln}\frac{R_i}{R_0}\right) - N_l''(\alpha_{ln})J_l'\left(\alpha_{ln}\frac{R_i}{R_0}\right)\right] - \frac{R_i}{r_0}\left[J_l''\left(\alpha_{ln}\frac{R_i}{R_0}\right)N_l'(\alpha_{ln}) - N_l''\left(\alpha_{ln}\frac{R_i}{R_0}\right)J_l'(\alpha_{ln})\right]\right\}^{-1}, \quad (22)$$

and at resonance, we have

$$\omega_0 = \frac{l\Omega_0}{\gamma_0}\gamma_{z0}^2 \pm \beta_{z0}\gamma_{z0}\left[\left(l\frac{\Omega_0}{\gamma_0}\gamma_{z0}\right)^2 - \alpha_{ln}^2\frac{c^2}{R_0^2}\right]^{1/2}, \quad (23)$$

$$k_z c = \frac{l\Omega_0}{\gamma_0}\gamma_{z0}^2\beta_{z0} \pm \gamma_{z0}\left[\left(l\frac{\Omega_0}{\gamma_0}\gamma_{z0}\right)^2 - \alpha_{ln}^2\frac{c^2}{R_0^2}\right]^{1/2},$$

and

$$\nu/\gamma_0 = \omega_b^2 r_0^2/2\gamma_0 c^2.$$

From Eq. (23), we require for resonance that $l\beta_{\phi 0}\gamma_{z0} > x_{ln}$.

B. TM coaxial mode

The fields for the TM coaxial waveguide modes can be determined from the E_z field with $B_z = 0$. This field is given by

$$E_z = \mathscr{C}_l(\beta_{ln} r/R_0)\exp i(l\phi + k_z z - \omega t), \quad (24)$$

where $\mathscr{C}_l$ has the same form as in Eq. (16). Applying the appropriate boundary conditions allows the determination of the eigenvalues β_{ln}, given by the solution to

$$J_l(\beta_{ln})N_l(\beta_{ln}R_i/R_0) - N_l(\beta_{ln})J_l(\beta_{ln}R_i/R_0) = 0, \quad (25)$$

with

$$(\beta_{ln}/R_0)^2 = \omega^2/c^2 - k_z^2.$$

Proceeding as in the TE mode, the following modified dispersion relation is obtained:

$$\omega^2 - k_z^2 c^2 - \beta_{ln}^2\frac{c^2}{R_0^2} = \frac{2\omega_b^2}{\gamma_0 D_l^2}(\omega\beta_{z0} - k_z c)^2\delta_{ln}^2\left[A_{ln}\mathscr{C}_l^2(y_{ln}) + B_{ln}\mathscr{C}_l(y_{ln})\mathscr{C}_l'(y_{ln}) + C_{ln}\mathscr{C}_l'^2(y_{ln})\right], \quad (26)$$

where

$$\begin{aligned}
\delta_{ln}^2 &= [\eta_0^2 y_{ln}^2\mathscr{C}_l'^2(\eta_0 y_{ln}) - \eta_i^2 y_{ln}^2\mathscr{C}_l'^2(\eta_i y_{ln})]^{-1},\\
A_{ln} &= l^2\left(\psi_l^2 - \frac{\Omega_0^2}{\gamma_0^2}\right) + y_{ln}^2\left(\frac{\psi_l^2}{(\omega\beta_{z0} - k_z c)^2} - 1\right)\left(\psi_l^2 - \frac{\Omega_0^2}{\gamma_0^2}\right),\\
B_{ln} &= -y_{ln} l(\Omega_0/\gamma_0)\psi_l,\\
C_{ln} &= y_{ln}^2\psi_l^2,
\end{aligned} \quad (27)$$

with

$$y_{ln} = \beta_{ln} r_0/R_0.$$

For *resonant* beam-waveguide mode interaction, the above dispersion relation can be simplified and a growth rate $\Gamma_{TM} \equiv Im\omega$ computed:

$$\frac{\Gamma_{TM}}{\omega_c(\nu/\gamma_0)^{1/3}} = \frac{\sqrt{3}}{(2\beta_{\phi 0})^{2/3}}\left(\frac{[l(\Omega_0/\gamma_0)\gamma_{z0})]^2 - \beta_{ln}^2 c^2/R_0^2}{(\Omega_0/\gamma_0)\omega_0\gamma_{z0}^2}\right)^{1/3}\left[h_{ln}^{TM}\left(1 - \frac{l^2}{y_{ln}^2}\right)\right]^{1/3}, \quad (28)$$

where

$$h_{ln}^{TM} = \frac{\pi}{2}y_{ln}\left[J_l\left(\beta_{ln}\frac{R_i}{R_0}\right)N_l(y_{ln}) - N_l\left(\beta_{ln}\frac{R_i}{R_0}\right)J_l(y_{ln})\right]\left[J_l(\beta_{ln})N_l(y_{ln}) - J_l(y_{ln})N_l(\beta_{ln})\right] \times \left\{\frac{R_0}{r_0}\left[J_l'(\beta_{ln})N_l\left(\beta_{ln}\frac{R_i}{R_0}\right) - N_l'(\beta_{ln})J_l\left(\beta_{ln}\frac{R_i}{R_0}\right)\right] - \frac{R_i}{r_0}\left[J_l'\left(\beta_{ln}\frac{R_i}{R_0}\right)N_l(\beta_{ln}) - N_l'\left(\beta_{ln}\frac{R_i}{R_0}\right)J_l(\beta_{ln})\right]\right\}^{-1} \quad (29)$$

and at resonance

$$\omega \simeq \omega_0 = l\frac{\Omega_0}{\gamma_0}\gamma_{z0}^2 \pm \beta_{z0}\gamma_{z0}\left[\left(l\frac{\Omega_0}{\gamma_0}\gamma_{z0}\right)^2 - \beta_{ln}^2\frac{c^2}{R_0^2}\right]^{1/2},$$

$$k_z c = l\frac{\Omega_0}{\gamma_0}\beta_{z0}\gamma_{z0}^2 \pm \gamma_{z0}\left[\left(l\frac{\Omega_0}{\gamma_0}\gamma_{z0}\right)^2 - \beta_{ln}^2\frac{c^2}{R_0^2}\right]^{1/2}, \tag{30}$$

and for resonance to occur, we require $l\beta_{\phi 0}\gamma_{z0} > y_{ln}$.

In Figs. 4–12, graphical resuts are presented of the linear growth rates for the waveguide-beam mode resonant interactions as given in Eqs. (21) and (28) as a function of various beam and system parameters. We find that an inner conductor for given beam properties and fixed outer conductor radius has very little effect unless the inner conductor is extremely close to the beam. With this in mind, we first present results for a hollow waveguide and show the growth rate dependence on harmonic number l, outer wall radius R_0, and axial beam velocity β_{z0}. We specifically display the results as a function of frequency over the spectrum examined in the experiment, i.e., X and Ka bands. Finally, we display the effects of the inner conductor. We normalize our growth rates to $\omega_c(\nu/\gamma_0)^{1/3} = (eB_0/m\gamma_0)(\nu/\gamma_0)^{1/3}$. Thus, for a given γ_0 and beam radius r_0, we see that as β_{z0} varies, B_0 varies appropriately according to Eq. (6). However, for the range of β_{z0} covered in our graphs, there is very little change in B_0, i.e., about 30 G out of 1680 G.

In Figs. 4–6, the results of the TE resonant interaction, Eq. (21), are presented for a hollow waveguide $R_i = 0$ as a function of various system parameters. In Fig. 4, the beam properties are fixed at $\gamma_0 = 6$, $\beta_{z0} = 0.2$, and $r_0 = 6$ cm. In Fig. 4(a), the $n = 1$ growth rate is plotted versus harmonic number l with r_0/R_0 as a parameter. We have only plotted the "backward" traveling wave (k_z^-, ω^-), as shown in Fig. 3. We see that for a given r_0/R_0 there is no resonant interaction for low harmonic numbers. The interaction begins when $l > x_{ln}/\beta_{\phi 0}\gamma_{z0}$. However, once resonance can occur, the linear growth is fairly constant for beams near the outer wall for $1 \leqslant l \leqslant 80$. In Fig. 4(b), r_0/R_0 is fixed at 0.8 and all radial mode numbers are examined for stability in the region $1 \leqslant l \leqslant 80$. We see that as the $n = 1$ mode growth rate falls at larger l, the $n = 2$ radial mode becomes unstable for $l \gtrsim 41$, and finally at $l \sim 75$, the $n = 1$, 2, and 3 modes are all unstable. Thus we expect a fairly broad spectrum of unstable modes once the condition for the $n = 1$ mode is satisfied. In Figs. 4(c) and 4(d), the results are plotted versus r_0/R_0 with harmonic number l a parameter. Again, the lack of resonance at low harmonic numbers is seen for beams located nearer to the outer wall.

In Figs. 5 and 6, the results are plotted as a function of frequency and specifically in the region from 0–20 and 20–40 GHz for comparison (qualitatively) with the experiment. In Fig. 5, the beam parameters are $\gamma_0 = 6$, $r_0 = 6$ cm, $r_0/R_0 = 0.8$, and $\beta_{z0} = 0.0$. For this case, we see that both the "forward" and "backward" unstable waves occur at exactly the same frequency; thus each point represents both the ω^- and ω^+ growth rates. The entire unstable spectrum is shown in Fig. 5(a) where we see the first unstable mode is $l = 7$ for $n = 1$, $l = 41$ for $n = 2$, and $l = 74$ for $n = 3$. The frequency region covered by X band is shown in Fig. 5(b) and that by Ka band in Fig. 5(c). Only the $n = 1$ radial mode is

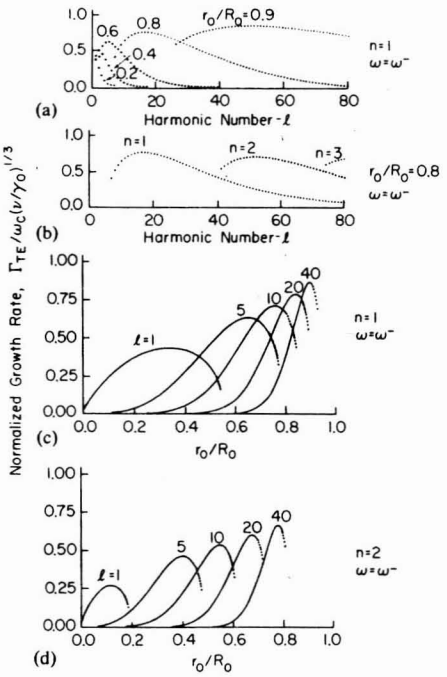

FIG. 4. Normalized TE growth rate [Eq. (21)] for beam properties $\gamma_0 = 6$, $\beta_{z0} = 0.2$, $r_0 = 6$ cm, and $R_i = 0.0$ vs (a) harmonic number l for $n = 1$, $\omega = \omega^-$ mode with r_0/R_0 a parameter, (b) harmonic number l for $r_0/R_0 = 0.8$, $\omega = \omega^-$ mode with n a parameter, (c) r_0/R_0 for $n = 1$, $\omega = \omega^-$ mode with l a parameter, and (d) r_0/R_0 for $n = 2$, $\omega = \omega^-$ mode with l a parameter.

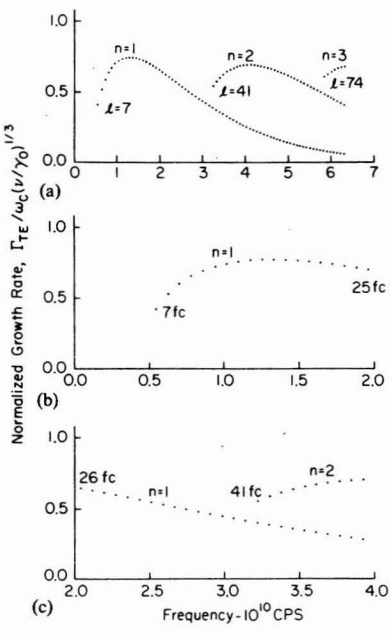

FIG. 5. Normalized TE growth rate [Eq. (21)] for beam properties $\gamma_0 = 6$, $\beta_{z0} = 0.0$, $r_0 = 6$ cm, $r_0/R_0 = 0.8$, $R_i = 0.0$ vs frequency. Note $\omega^- = \omega^+$. (a) Full spectrum for $1 \leqslant l \leqslant 80$, (b) 0–20 GHz, and (c) 20–40 GHz.

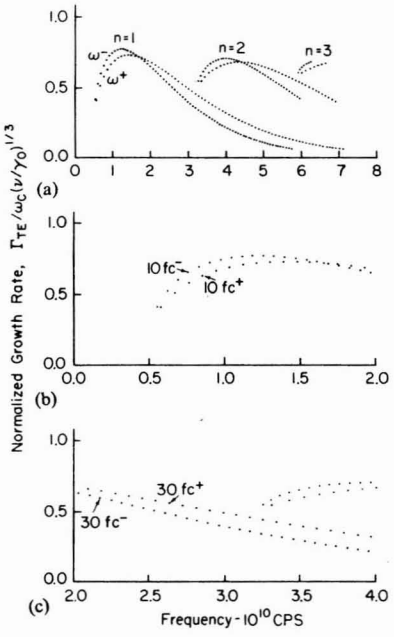

FIG. 6. Normalized TE growth rate [Eq. (21)] for beam properties $\gamma_0 = 6$, $\beta_{z0} = 0.2$, $r_0 = 6$ cm, $r_0/R_0 = 0.8$, $R_i = 0.0$ vs frequency. Note $\omega^- \neq \omega^+$. (a) Full spectrum for $1 \leqslant l \leqslant 80$, (b) 0–20 GHz, and (c) 20–40 GHz.

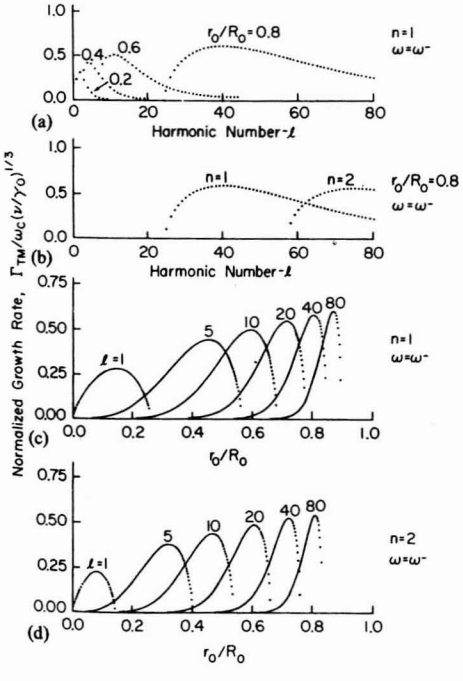

FIG. 7. Normalized TM growth rate [Eq. (28)] for beam properties $\gamma_0 = 6$, $\beta_{z0} = 0.2$, $r_0 = 6$ cm, and $R_i = 0.0$ vs (a) harmonic number l for $n = 1$, $\omega = \omega^-$ mode with r_0/R_0 a parameter, (b) harmonic number l for $r_0/R_0 = 0.8$, $\omega = \omega^-$ mode with n a parameter, (c) r_0/R_0 for $n = 1$, $\omega = \omega^-$ mode with l a parameter, and (d) r_0/R_0 for $n = 2$, $\omega = \omega^-$ mode with l a parameter.

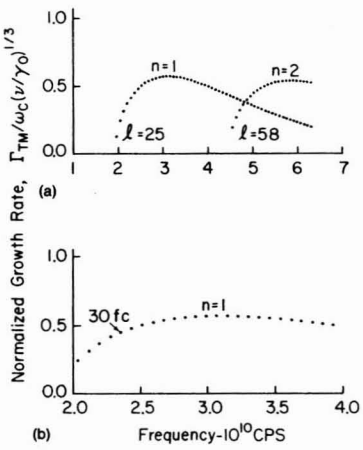

FIG. 8. Normalized TM growth rate [Eq. (28)] for beam properties $\gamma_0 = 6$, $\beta_{z0} = 0.0$, $r_0 = 6$ cm, $r_0/R_0 = 0.8$, $R_i = 0.0$ vs frequency. Note $\omega^- = \omega^+$. (a) Full spectrum for $1 \leqslant l \leqslant 80$ and (b) 20–40 GHz.

observed in the less than 20-GHz region while both the $n = 1$ and $n = 2$ radial modes are seen in the 20–40-GHz region.

In Fig. 6, the beam's axial velocity is $\beta_{z0} = 0.2$ while all other beam parameters remain the same as in Fig. 5. Now the ω^- and ω^+ unstable modes are seen not to be coincident but are shifted below and above the $l\omega_c$ frequency. Explicitly, the $l = 10$ mode is labeled in Fig. 6(b) while the $l = 30$ mode is labeled in Fig. 6(c). Thus, when $\beta_{z0} = 0$, the points coalesce, whereas for finite β_{z0}, the two modes ω^- and ω^+ separate with the separation becoming greater with larger

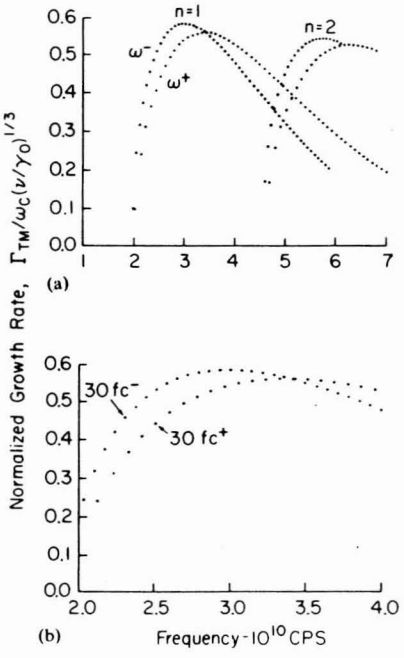

FIG. 9. Normalized TM growth rate [Eq. (28)] for beam properties $\gamma_0 = 6$, $\beta_{z0} = 0.2$, $r_0 = 6$ cm, $r_0/R_0 = 0.8$, $R_i = 0.0$ vs frequency. Note $\omega^- \neq \omega^+$. (a) Full spectrum for $1 \leqslant l \leqslant 80$ and (b) 20–40 GHz.

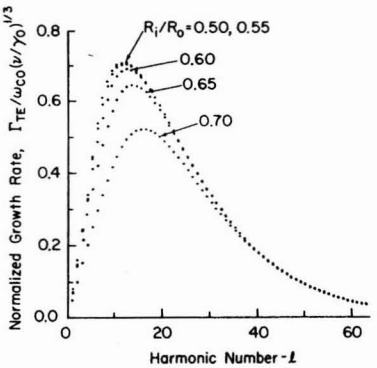

FIG. 10. Normalized TE growth rate [Eq. (21)] for beam properties $\gamma_0 = 6$, $\beta_{z0} = 0.2$, $r_0 = 6$ cm, $r_0/R_0 = 0.75$ vs harmonic number l for the $n = 1$, $\omega = \omega^-$ mode with inner conductor radius a parameter, R_i/R_0. (ω_{c0} is value of ω_c when $\beta_{z0} = 0.0$.)

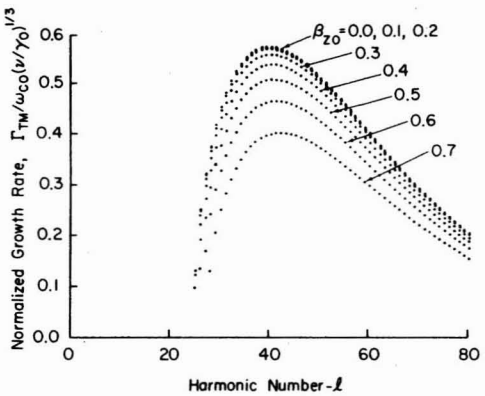

FIG. 12. Normalized TM growth rate [Eq. (28)] for beam properties $\gamma_0 = 6$, $r_0 = 6$ cm, $r_0/R_0 = 0.75$, $R_i/R_0 = 0.5$ vs harmonic number l for the $n = 1$, $\omega = \omega^-$ mode with axial velocity β_{z0} a parameter. (ω_{c0} is value of ω_c when $\beta_{z0} = 0.0$.)

β_{z0}. We still may observe a strong interaction at a given frequency; however, from these results, they would have to be interpreted as different l numbers. As an example, in Fig. 6(c), we see the $l = 30^-$ mode is very close to the $l = 25^+$ mode, etc.

In Figs. 7–9, the results of the TM resonant interaction, Eq. (28), are presented for a hollow waveguide, $R_i = 0$. They are displayed in exactly the same format as the TE results. The most significant difference is that resonant interaction does not occur until larger harmonic numbers are reached, i.e., at higher frequencies for the same beam and conducting wall geometry. In fact, for $r_0/R_0 = 0.8$, no unstable modes are seen for less than about 20 GHz. The magnitude of the growth rates are the same as for the TE mode. In combining the results of the TE and TM resonant interaction, we would conclude that the less than 20-GHz spectrum involves unstable modes that are TE in nature and only the $n = 1$ radial mode, whereas the 20–40-GHz spectrum involves TE and TM modes with $n = 1$ and 2 for the TE waves and $n = 1$ for the TM waves. Including the effects of finite β_{z0}, we would expect some discreteness in the power spectrum in the X-band frequency region but considerably less discreteness in the Ka-band frequency region.

In Figs. 10 and 11, the effects of an inner conductor on the TE and TM resonant interaction are shown. The beam parameters are $\gamma_0 = 6$, $r_0 = 6$ cm, $\beta_{z0} = 0.2$, and $r_0/R_0 = 0.75$ in both figures. Also, only the results for the $n = 1$ and ω^- mode are displayed. For the TE mode, Fig. 10, the hollow waveguide result is effectively obtained for $R_i/R_0 \lesssim 0.65$, and substantial change is observed only when $0.7 < R_i/R_0 < 0.75$, that is, when the inner conductor is at the beam radius. For the TM mode, Fig. 11, the inner conductor has to be even closer before any substantial change is seen.

In Fig. 12, an appropriately normalized growth rate is plotted to show the effect of finite β_{z0}. Though there is a decrease in growth rate as β_{z0} increases, there is little change in the spectrum for the choice of system parameters chosen except as indicated above.

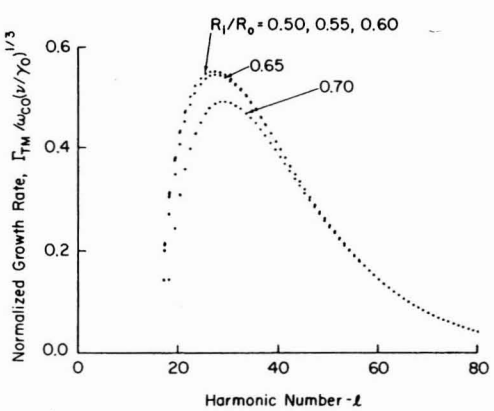

FIG. 11. Normalized TM growth rate [Eq. (28)] for beam properties $\gamma_0 = 6$, $\beta_{z0} = 0.2$, $r_0 = 6$ cm, $r_0/R_0 = 0.75$ vs harmonic number l for the $n = 1$, $\omega = \omega^-$ mode with inner conductor radius a parameter, R_i/R_0. (ω_{c0} is value of ω_c when $\beta_{z0} = 0.0$.)

III. EXPERIMENT

The experiments were performed at the University of Maryland's Charged Particle Beam Facility. The apparatus used is shown schematically in Fig. 13. A coil pair forms the upstream half of a cusp magnetic field, and a solenoidal set of

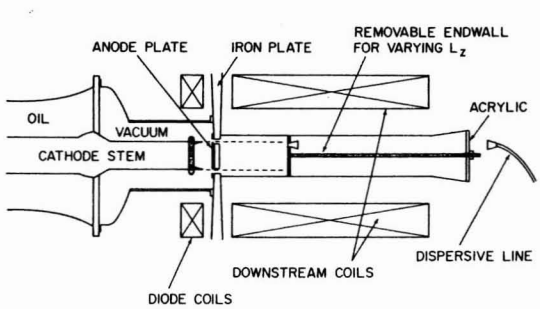

FIG. 13. General experimental configuration.

coils located around the downstream drift chamber provides the other half of the cusp. The solenoidal coils also provide a uniform field region where the beam propagates. Here beam modes couple with the modes of the hollow waveguide formed by the drift chamber. A soft iron plate has been inserted between these two coils to shorten the cusp field transition region.

In operation, a hollow cylindrical beam of 25-ns duration, full width at half-maximum (FWHM), is emitted from the circular knife-edge cathode of 6-cm radius. The cathode is made of tantilum or carbon. The electrons travel approximately 7.5 cm to a brass anode disc attached to the iron plate. The anode disc has an annular slit of 6-cm mean radius through which the electrons pass into the downstream region. During this transversal from the cathode to the downstream region, the electrons feel a $v_z \times B_r$ force, which acts to convert the axial velocity of the beam electrons into rotational velocity, thereby producing a rotating ring of electrons. Some control over the amount of electrons propagating into the downstream region may be achieved by varying the annular slit width, while control over the energy of the particles may be achieved by varying the diode voltage.

Typical values used in the experiment were a diode voltage of 2.5 MV and a diode current of 10 kA. The magnetic field was varied over the range 800–1500 G. A vacuum of about 10^{-5} Torr was maintained upstream and downstream of the cusp transition. The hollow rotating E layer propagating in the downstream region (typically, 2.5 MeV, 1–2 kA, 2–5 ns) is guided by the uniform magnetic field provided by the solenoidal coils. The chamber itself is a 3-m long, 15-cm diam aluminum cylinder, which forms the permanent outer conducting boundary for all experiments. Various inner conductors may be inserted into the downstream drift chamber on axis.

The radiated power spectrum for the experiment is obtained using the setup shown in Fig. 13. The downstream end of the drift chamber is flared to allow a smooth transition of TE and TM waveguide modes into free-space TEM modes. A pair of receiving horns and dispersive lines (X band, 7–12 GHz and Ka band, 24–40 GHz) of length 34 and 24 m, respectively, are placed a known distance beyond the acrylic endplate. Microwaves are transmitted through these lines through calibrated attenuators to calibrated detectors. The total radiation may be calculated by taking into account the solid angle subtended by the receiving horns and the attenuation curves for the dispersive lines. The frequency content may be determined from their dispersion characteristics.

A. Hollow guide experiments

The coupling of unstable beam modes into the TE and TM waveguide modes of an open-ended hollow cylindrical waveguide (15-cm diam) has been studied extensively. The total radiated power in X band has been measured as a function of applied cusp magnetic field, and is plotted in Fig. 14(a) for different injected beams with peak energies of 2.0 and 2.5 MV, respectively. Peak injected current in both cases is in the range of 1–2 kA. It is interesting to note that the

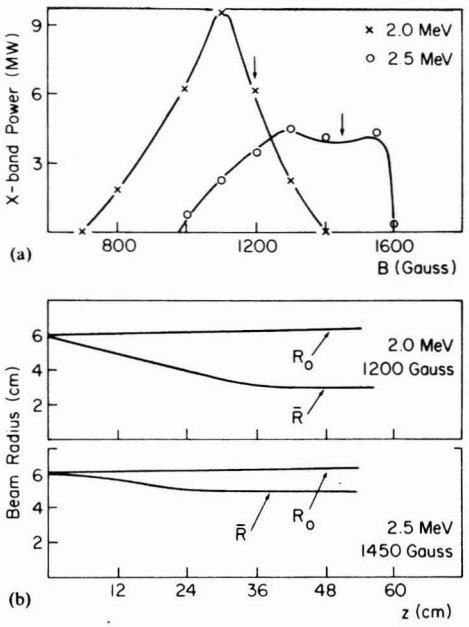

FIG. 14. (a) Radiated power in X-band (7–12 GHz) vs cusp magnetic field for two different peak electron beam energies. (b) Mean radius $\bar{R}$ and outer radius R_0 of the beam as a function of axial position downstream of the cusp.

cutoff of radiation occurs at higher applied magnetic fields for the higher energy cases, a result consistent with the fact that higher cusp fields are required, in this case, to prevent beam transmission through the cusp.[16] It is also evident that the highest radiated power is observed for the lower beam energy. The spectral content of this radiation is discussed in Sec. III.

Time integrated photographs of the light emitted when the downstream beam strikes a graphite-covered acrylic beamstop have been used to measure the mean beam radius $\bar{R}$ and outer radius R_0, as a function of axial position in the drift chamber. Results of these studies for the 2.0- and 2.5-MeV cases are plotted in Fig. 14(b). The magnetic field was chosen so that the axial beam velocity in each case was approximately 0.3 c. It is readily seen that the loss of mean beam radius as the beam propagates is much greater in the 2.0-MeV case than in the 2.5-MeV case. This result is consistent with the higher power levels observed for the 2.0-MeV case. If the total loss in mean beam radius is due to radiated energy, the total radiated power should be about 10^9 W.

B. Effect of inner conducting boundaries

In order to study the effect of different conducting boundary systems on the radiated power, three different configurations were used. The conductors were inserted in the downstream drift chamber on axis. These were (1) a solid inner conductor of 5.0-cm-diam, (2) a solid inner conductor of 7.5-cm-diam, and (3) a 8.75-cm-diam "squirrel cage" conductor designed to allow image charge but not azimuthal image currents. Previous experiments have shown that such a configuration provides axial focusing of the beam elec-

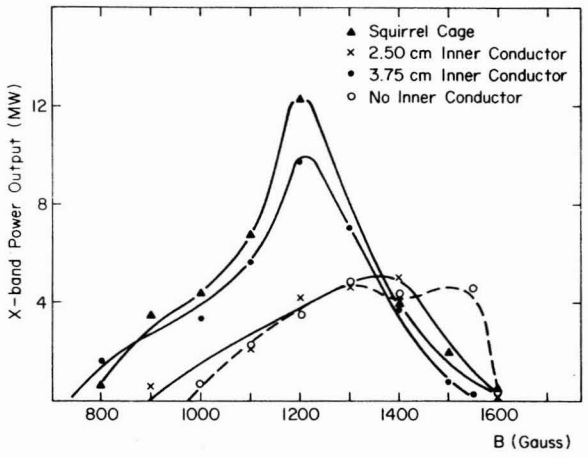

FIG. 15. Radiated power in X band for various conducting boundary configurations.

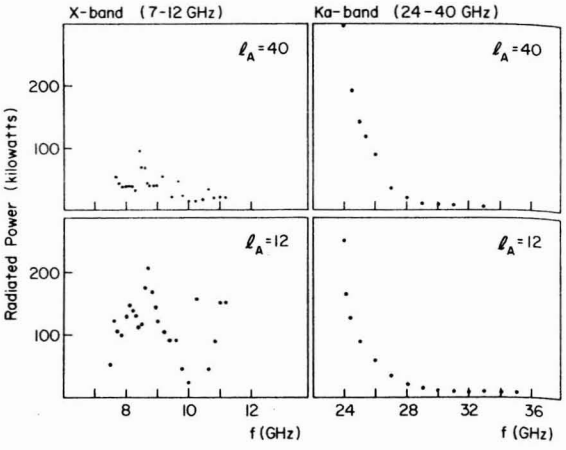

FIG. 16. Typical radiated power spectra in X band and Ka band for the $l_A = 12$ and $l_A = 40$ anodes.

trons.[15] The total radiated power in X band has been measured as a function of applied cusp field for each of these configurations and is plotted in Fig. 15. It is evident that the highest radiated power levels are observed when an inner conductor is present and that larger diameter inner conductors seem to result in greater radiation production. Although the highest radiated powers are observed in the squirrel cage configuration, it is not clear from the results whether this is due to the changed boundary conditions or simply the larger diameter of the squirrel cage conductor.

C. Effects of preloaded azimuthal density structure

By passing the beam through an anode plate with a given number of azimuthally spaced transmission apertures located at the beam radius, a preloaded beam density structure may be imparted to the beam prior to the cusp field. In this manner, some control over the beam-waveguide mode coupling may be exercised. In the experiment, two anode plates, with $l_A = 12$ and $l_A = 40$ apertures, respectively, were used. As the electron cyclotron frequency is about 800 MHz in these experiments, the $l_A = 12$ anode was chosen to maximize radiation in the X band while the $l_A = 40$ anode was designed to maximize Ka-band radiation. The actual beam transmission area was 28% higher for the $l_A = 12$ anode than for the $l_A = 40$ anode. Typical power spectra and plots of the total power in each band as a function of applied magnetic field are shown in Figs. 16 and 17, respectively. Several features are apparent from these measurements.

(1) As expected, the radiated power in X band is greater for the $l_A = 12$ case than for the $l_A = 40$ case, while the radiated power in Ka band is greater for the $l_A = 40$ case despite the reduced anode transmission area.

(2) While some control over the radiated power spectrum has been achieved, in both cases the greatest radiated power appears to be at frequencies between 12 and 24 GHz. This result is consistent with the theoretical studies that indicate that the TM modes do not occur for frequencies below about 16 GHz.

(3) To exert greater control over the radiated power spectrum, it may be necessary to tailor the downstream waveguide towards the excitation of a particular mode.

D. Effect of finite axial length

In an attempt to fix the axial wavelength of the radiation and thereby control the radiated power spectrum, a movable conducting endwall was introduced into the system, as shown in Fig. 13. A small rectangular aperture in the endwall was used to couple radiation out of the fixed length cavity where it propagated to the end of the system guided by the 15-cm drift tube.

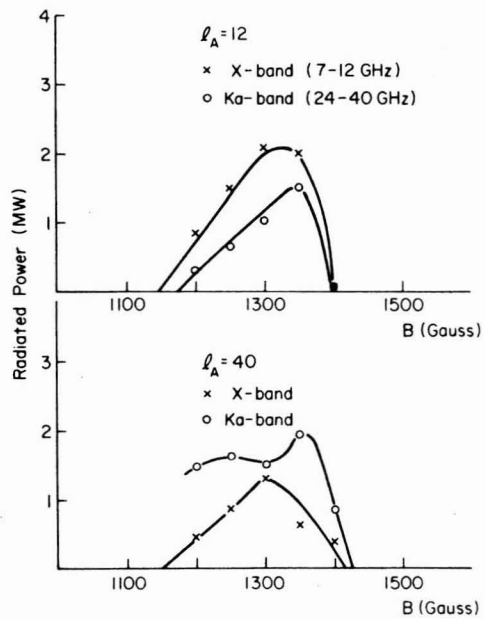

FIG. 17. Total radiated power in X band and Ka band vs cusp magnetic field for the $l_A = 12$ and $l_A = 40$ anodes.

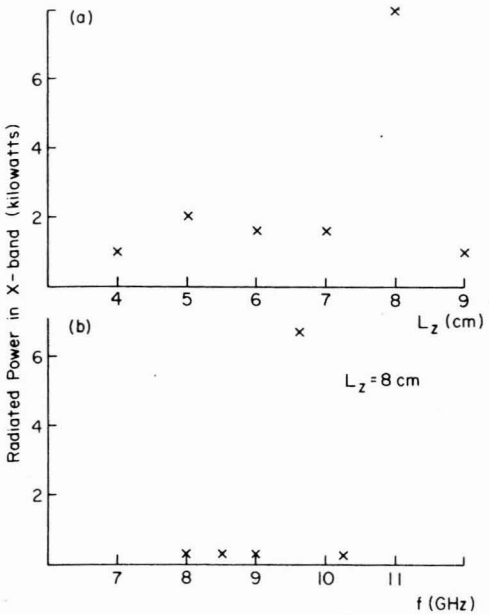

FIG. 18. Radiated power in X band for a finite length cylindrical drift chamber. (a) Radiated power vs axial length of the chamber. (b) Power spectrum at $L_z = 8$ cm.

Total radiated power in the X band as a function of the axial cavity length L_z is plotted in Fig. 18(a). It is evident that radiated power is maximum at $L_z = 8$ cm. The radiated output spectrum in X band is plotted for this case in Fig. 18(b). While further work remains to be done in this area, it is apparent that, by fixing the axial length of the system and thereby the axial wavelength of the cavity, individual modes may be excited. It is important to note, however, that total radiated power is much lower in this case, perhaps due to a relatively poor efficiency of coupling the radiation out of the system.

IV. CONCLUSIONS

The major conclusions to be drawn from this work are: (1) The theoretical analysis of possible resonant interactions between beam modes and TE and TM waveguide modes of the drift chamber predicts a broadband radiation spectrum in reasonable agreement with experimental observations. (2) Experimental measurements of the radiation spectrum indicate that substantial radiated power is produced at frequencies in the range 12–24 GHz, a result consistent with the theoretical analysis, which shows that the TM modes should begin to be observed at about 16 GHz. (3) It is apparent that some control over the radiation spectrum may be achieved by either providing a preloaded azimuthal density structure to the beam or by using a finite length drift chamber to fix the axial wavelength of the radiation.

ACKNOWLEDGMENTS

It is a pleasure to acknowledge the assistance of M. J. Rhee and M. Reiser in this work. Technical assistance was provided by D. Cohen and J. Pyle. This work was supported by the Air Force Office of Scientific Research and the University of Maryland Computer Science Center.

[1]M. Friedman, Appl. Phys. Lett. **26**, 366 (1975).
[2]Y. Carmel, J. Ivers, R. E. Kribel, and J. Nation, Phys. Rev. Lett. **33**, 1278 (1974).
[3]N. F. Kovalev, M. I. Petelin, M. D. Kaiser, A. V. Smorgonskii, and L. E. Tsopp, Zh. Eksp. Teor. Fiz. Pis'ma Red. **18**, 232 (1973) [Sov. Phys.-JETP].
[4]G. Bekefi and T. Orzechowck, Phys. Rev. Lett. **37**, 379 (1976).
[5]A. Palevsky and G. Bekefi, Phys. Fluids **22**, 986 (1979).
[6]L. Barnett, K. Chu, J. Baird, and V. Granatstein, Bull. Am. Phys. Soc. **24**, 1067 (1979).
[7]See, for example, Bull. Am. Phys. Soc. **24**, 1066 (1979).
[8]V. L. Granatstein, R. K. Parker, and P. Sprangle, Proc. Int. Topical Conference on Electron Beam Research and Technology, Albuquerque, 1975, Vol. II, p. 401 (unpublished).
[9]W. W. Destler, D. W. Hudgings, M. J. Rhee, S. Kawasaki, and V. L. Granatstein, J. Appl. Phys. **48**, 3291 (1977).
[10]A. Faltens, G. R. Lambertson, J. M. Peterson, and J. B. Rechen, Proceedings of the IXth International Conference on High Energy Accelerators, Stanford, 1974, p. 226 (unpublished).
[11]C. H. Dustmann, W. Heinz, H. Krauth, L. Steinbock, and W. Zernial, in Ref. 10, p. 250.
[12]J. Fink, W. Herrmann, W. Ott, and J. M. Peterson, in Ref. 10, p. 223.
[13]P. Sprangle, J. Appl. Phys. **47**, 2935 (1976).
[14]H. Uhm and R. C. Davidson, J. Appl. Phys. **49**, 593 (1978).
[15]Y. Goren, H. Uhm, and R. C. Davison, J. Appl. Phys. **49**, 3789 (1978).
[16]M. J. Rhee and W. W. Destler, Phys. Fluids **17**, 1574 (1974).